AIAA JOURNAL
Vol. 39, No. 4, April 2001

Random Packing of Heterogeneous Propellants

G. M. Knott,* T. L. Jackson,† and J. Buckmaster‡
University of Illinois at Urbana–Champaign, Urbana, Illinois 61801

A random packing algorithm is implemented to construct numerically models of heterogeneous propellants. These models consist of random distributions of spheres in a periodic cube. The spheres can have various sizes, randomly assigned if desired. Packing fractions are calculated for a bimodal model (spheres of two different sizes) and compare well with old experimental data for steel shot. Slices through the cube define surfaces that represent propellant surfaces, and the stoichiometry of these surfaces is a stochastic variable. Several realizations of the propellant cube are constructed and variations in surface stoichiometry are examined using histograms and Fourier series. A sample flame calculation is presented and solved using data defined by a single surface realization.

Introduction

We are concerned with heterogeneous propellants in which particles of ammonium perchlorate (AP) are randomly imbedded in a fuel binder. A slice through such a propellant defines a surface, partly AP, partly fuel, which defines data for a three-dimensional combustion field. It is well established that the nature of this combustion field and the heat that it generates (which controls the surface regression, the burning rate) depends on these data. Accordingly, any complete description of propellant burning must incorporate an algorithm that determines the propellant morphology, the manner in which the particles are packed.

The problem of propellant flames is one that has been discussed for many years. There have been creative efforts to define meaningful one-dimensional models, homogenized false propellants that in some way reflect the true heterogeneous nature and its statistical properties,[1,2] and flame configurations have been drawn, rooted in physical insight, that have played an important role in the discussion of propellant behavior and in the interpretation of experimental results, for example, see Refs. 3 and 4. What has been missing, however, are attempts at three-dimensional simulations that account for at least the minimum chemical ingredients (the AP decomposition flame, the AP/binder diffusion flame, and its edge), the random nature of the propellant morphology, the uneven regression of the propellant surface, the different mechanical properties (density and thermal diffusivity) of the AP and binder, and the field processes (diffusion and flow) in the two phases.

There is no doubt that available computational power now makes it possible to consider such calculations, and it is reasonable to argue that there are important fundamental questions of propellant burning that will not be answered until such calculations are successfully performed. They are difficult, however, and which details are important and which are not is not transparent. For this reason, we think it best to take a cautious approach, adding the ingredients incrementally. Morphology affords an example. Our first attempt at three-dimensional calculations uses a lattice propellant, a regular bimodal array of spheres,[5,6] a natural choice in the absence of a random packing algorithm. However, if one compares slices through such a propellant with the slices generated in the present work there are significant differences, and we believe that some of the surfaces defined by the lattice are physically unrealistic and should be avoided.

Algorithms for periodic propellants in which the particles are spherical are quite simple; this is true even though spheres of various sizes must be used to achieve a stoichiometric mix of AP and binder. Such is not the case, however, for a random pack. Fortunately, the packing problem is one that is of interest beyond the narrow boundaries of propellant combustion and has been studied both experimentally and numerically.

We start with a brief description of some experiments on the packing of steel shot, reported in 1961 (Ref. 7). Bimodal packing is investigated in which spheres of diameter 0.124 in. (mesh 7) are packed with smaller spheres. The smaller spheres are defined by Table 1.

The packing volume is defined as the volume of the particles plus the interstitial volume. The packing fraction ρ (the fraction of the packing volume that is particles) is measured as a function of the volume fraction of fine particles (the volume of fine particles divided by the total volume of particles); the results are reproduced in Fig. 1.

When the particle volume fraction is 0 or 100%, the packing is monomodal and the packing fraction is approximately 0.625. Higher packing fractions are achieved for bimodal packs and the greater the disparity in sizes, the greater the packing fraction. In all cases, the maximum occurs at approximately 30% fine, 70% coarse. The largest packing fraction implied by this data is 0.8594. This is achieved by taking a monomodal pack and packing the interstices with a monomodal pack of vanishingly small spheres so that the packing fraction is

$$0.625 + 0.375 \times 0.625$$

The corresponding percentage of fine particles is 27.36%.

Typically, the packing fractions achieved are smaller than those that can be obtained using a lattice pack. Thus, a face-centered cubic lattice (monomodal) has a packing fraction of 0.7405, and the bimodal pack (spheres of relative size 1 and 0.35) discussed in Refs. 5 and 6 has a packing fraction of 0.7653. In contrast, the packing fraction required for a real AP propellant is approximately 0.80.

A numerical strategy (a packing algorithm) that we find is capable of duplicating McGeary's[7] data has been described in a number of papers by Lubachevsky and Stillinger[8] and Lubachevsky et al.[9] The strategy is simple, but ingenious.

We start with a periodic array of cubes, and in one of these cubes (hence, mirrored in all of its neighbors) we randomly place N points, each of which is randomly assigned a velocity. These points are kernels for the spheres that will eventually pack the cube. To produce spheres of different sizes the points are partitioned into M classes, so that

$$N = \bigcup_{i=1}^{M} N_i \tag{1}$$

M is the number of sizes that will be generated, so that $M = 2$ for a bimodal pack. The defining characteristic of each partition is that around each point in the partition a sphere grows at a rate $a_i t$. Specification of each a_i defines the relative sphere diameters in the

Received 11 February 2000; revision received 9 June 2000; accepted for publication 27 June 2000.

*Graduate Student, Department of Mechanical and Industrial Engineering, 1206 West Green Street; gknott@uiuc.edu.

†Research Scientist, Center for the Simulation of Advanced Rockets, 1304 West Springfield Avenue; tlj@csar.uiuc.edu.

‡Professor, Department of Aeronautical and Astronautical Engineering, 104 South Wright Street; limey@uiuc.edu. Associate Fellow AIAA.

Table 1 Mesh number/diameter data from Ref. 7

Mesh no.	Diameter, in. (cm)
7	0.124 (0.315)
20	0.036 (0.091)
30	0.026 (0.066)
40	0.019 (0.048)
60	0.011 (0.028)
80	0.0075 (0.019)
100	0.0065 (0.017)

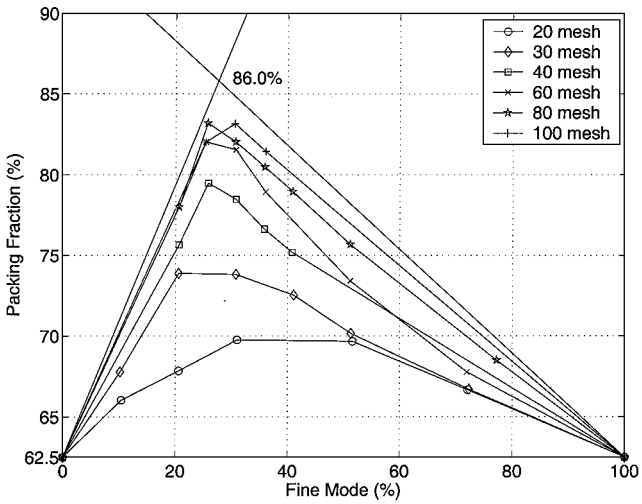

Fig. 1 McGeary's data for packing fraction.[7] McGeary plots the packing volume v for a fixed particle volume of 62.5, on a linear scale, and the packing fraction is $62.5/v \times 100\%$, plotted on a nonlinear scale. The packing fraction is shown here on a linear scale.

pack, and this specification may be random or determinate. Thus, for $t > 0$ we have spheres moving in the cube, and these will collide; a collision algorithm is an essential part of the picture. This algorithm conserves momentum but it does not conserve energy. A rebound component is added to the postcollision velocities of each collision pair, directed along the line of centers, and this has two effects: It ensures that the pairs do not stay in contact despite their growth, so that all collisions are discrete; and the added energy forces the particles into tight spaces, is the element of violence characteristic of mechanical packing. In due course, the spheres jam against each other, the time between collisions goes to zero, and the pack is defined.

A brief description of the algorithm may be found in Ref. 8, but it is useful, we believe, to enlarge on it and make it more accessible to the propellant community.

Packing Algorithm

Consider a unit cube and its 26 contiguous neighbors. These can be identified by the triple (p, q, r) where p, q, and r have the values $0, \pm 1$ and are the coordinates of the center of each cube relative to the center of the primary cube (henceforth, the cube). The N points, labeled with i $(i = 1, \ldots, N)$ are assigned to random locations in the cube, each point with random initial velocity of magnitude less than 1. Apart from the diameters, the state of the system at any time is defined by the state vector

$$\boldsymbol{S} = (\boldsymbol{r}_i, \boldsymbol{v}_i), \qquad i = 1, \ldots, N \tag{2}$$

where $\boldsymbol{r}_i$ is the position of the center of the ith sphere and $\boldsymbol{v}_i$ is its velocity. (A sphere is only within the cube if its center is in the cube.) The diameter of the ith sphere is equal to $a_i t$ where a_i takes on one of M values, according to the partition.

For the most part, the state evolves simply because each position vector changes according to the rule

$$\frac{\mathrm{d}\boldsymbol{r}_i}{\mathrm{d}t} = \boldsymbol{v}_i \tag{3}$$

where $\boldsymbol{v}_i$ is a constant. However, at discrete times an event occurs, and the state vector jumps. There are two kinds of events: exit of a particle through a face of the cube, with the corresponding entry of a periodic partner at the opposite face, and a collision. Collisions occur either between spheres that are in the cube (contact collisions) or between one sphere that is in the cube and one that is not. Because the latter has a periodic partner inside the cube, this is equivalent to collision at a distance, a remote collision. The algorithm must do the following: Given $\boldsymbol{S}$ following an event at $t = t_1$ we need to calculate t_2, the time of the next event, and the subsequent new state following that event. The chain of such events is followed (in number 10^5 or so) until no significant changes in the packing fraction occur because the particles are closely packed.

Collision Times

Consider the particles i and j. We can calculate the time to contact collision between these particles in the following fashion. The spheres are located at

$$\boldsymbol{r}_{i1} + \boldsymbol{v}_i \Delta t, \qquad \boldsymbol{r}_{j1} + \boldsymbol{v}_j \Delta t \tag{4}$$

where $\boldsymbol{r}_{i1}$ and $\boldsymbol{r}_{j1}$ are the positions at $t = t_1$ and Δt is the elapsed time. The collision occurs (if it does) when the separation distance is the average of the instantaneous diameters, that is, when

$$|\boldsymbol{r}_{i1} + \boldsymbol{v}_i \Delta t - \boldsymbol{r}_{j1} - \boldsymbol{v}_j \Delta t| = \tfrac{1}{2}(a_i t_1 + a_i \Delta t + a_j t_1 + a_j \Delta t) \tag{5}$$

This is a quadratic in Δt that will have complex roots (no collision), two negative roots (past "collision"), or two positive roots. (Real roots of different signs are not possible because the two particles cannot be overlapping.) In the latter case, we set the collision time $\chi(i, j)$ equal to the smaller of the positive roots, otherwise we set $\chi(i, j) = \infty$. Because the matrix $\chi(i, j)$ is symmetric, only the times for the half matrix $i \le j$, $j = 1, \ldots, N$, have to be calculated.

Remote collision times are calculated with the use of a small modification. Consider, for example, the collision between the ith sphere in the cube and the jth sphere in the neighboring cube $(-1, 1, 0)$. The latter sphere is located at

$$\boldsymbol{r}_j + (-1, 1, 0) = \boldsymbol{r}_{j1} + \boldsymbol{v}_j \Delta t + (-1, 1, 0) \tag{6}$$

and this is used instead of $\boldsymbol{r}_j$ in Eq. (5) to calculate the collision time; this has to be done for all i and j. However, the collision time matrix defined in this way is the transpose of the matrix defined by the mirror cube $(1, -1, 0)$ and so, although there are 26 neighboring cubes, these calculations only have to be done for 13 of them. Thus, $13\frac{1}{2}$ collision matrices have to be calculated, and the minimum of all of the matrix elements identified. This is the time to the next collision.

Exit Times

Assume that the faces of the cube (three pairs) are located at $x = 0, 1$; $y = 0, 1$; and $z = 0, 1$. Because the components of the position of the ith particle are

$$x_i = x_{i1} + v_{ix} \Delta t, \ldots \tag{7}$$

the times at which it crosses these planes are

$$\Delta t = -\frac{x_{i1}}{v_{ix}}, \ \frac{1 - x_{i1}}{v_{ix}}, \ -\frac{y_{i1}}{v_{iy}}, \ \frac{1 - y_{i1}}{v_{iy}}, \ -\frac{z_{i1}}{v_{iz}}, \ \frac{1 - z_{i1}}{v_{iz}} \tag{8}$$

and the exit time $\eta(i)$ is the smallest of these. This has to be calculated for all i.

Updating $\boldsymbol{S}$

The next event, following the one at $t = t_1$, occurs at

$$t = t_2 = t_1 + \Delta t_* \tag{9}$$

where Δt_* is the minimum of all collision times and exit times. If Δt_* is defined by a collision, the collision partners i_* and j_* are identified. All position vectors are updated, that is,

$$\boldsymbol{r}_{i2} = \boldsymbol{r}_{i1} + \Delta t_* \boldsymbol{v}_i \tag{10}$$

and the collision algorithm determines new values of $\boldsymbol{v}_{i_*}$ and $\boldsymbol{v}_{j_*}$. The other velocities are unchanged.

If $\triangle t_*$ is defined by an exit, an exit particle i_* and an exit face are identified. There are no changes in the $\boldsymbol{v}_i$, and the position vectors are updated as in Eq. (10) with an additional increment of $(\pm 1, 0, 0)$, $(0, \pm 1, 0)$, and $(0, 0, \pm 1)$ to $\boldsymbol{r}_{i_*}$, according to the exit face.

Updating Event Matrices

At this point the entire process can be repeated. However, the calculation of the new values of $\chi(i, j)$ and $\eta(i, j)$ is, in most cases, trivial because

$$\chi(i, j) \rightarrow \chi(i, j) - \triangle t_*, \qquad \eta(i) \rightarrow \eta(i) - \triangle t_* \tag{11}$$

except for those entries that involve the particles i_* and j_*, or just i_* alone, that were affected by the event. Thus, for the contact collisions, $\chi(i_*, j) = \chi(j, i_*)$ must be recalculated for all j to replace the values $\chi(i, i_*)$ for $i \leq i_*$ and $\chi(i_*, j)$ for $j > i_*$, and the same must be done for the particle j_*. Also, $\chi(i_*, j)$ and $\chi(j_*, j)$ must be recalculated for all j for the 13 remote collision matrices. Exit times must also be recalculated for i_* and j_*.

A strategy that is useful for speeding up the calculations is to search for collision partners of i only in some restricted neighborhood of $\boldsymbol{r}_i$. An occasional overlap check (no point should lie simulaneously in more than one particle) can ensure that a large enough neighborhood has been chosen.

Another short cut is to ignore exit events and reset $\boldsymbol{S}$ only after collisions. This fails to account for collisions between particles originating in the cube and those originating outside of the cube and its 26 neighbors, but the chances of such collisions being the first are remote. With this strategy, after each collision the cube (and, hence, its neighbors) is repopulated using the current position of all N particles and appropriate periodic mappings.

Collision Dynamics

Consider two particles i and j that collide that have velocities $\boldsymbol{u}_i$ and $\boldsymbol{u}_j$ immediately preceding the collision and velocities $\boldsymbol{v}_i$ and $\boldsymbol{v}_j$ immediately after. The positions of the particles $\boldsymbol{r}_i$ and $\boldsymbol{r}_j$ are known at the moment of collision.

The velocity components in the tangent plane at the point of contact are unaffected, that is to say,

$$(\boldsymbol{u}_i - \boldsymbol{v}_i) \times (\boldsymbol{r}_i - \boldsymbol{r}_j) = (\boldsymbol{u}_j - \boldsymbol{v}_j) \times (\boldsymbol{r}_i - \boldsymbol{r}_j) = 0 \tag{12}$$

Momentum is conserved,

$$m_i(\boldsymbol{v}_i - \boldsymbol{q}) + m_j(\boldsymbol{v}_j - \boldsymbol{q}) = 0 \tag{13}$$

where m_i and m_j are the individual masses and

$$\boldsymbol{q} = \frac{m_i \boldsymbol{u}_i + m_j \boldsymbol{u}_j}{m_i + m_j} \tag{14}$$

is the velocity of the center of mass prior to collision.

If energy were conserved, this would complete the determination of $\boldsymbol{v}_i$ and $\boldsymbol{v}_j$ and, in particular, the components along the line of centers

$$\boldsymbol{v}_i \cdot (\boldsymbol{r}_i - \boldsymbol{r}_j), \qquad \boldsymbol{v}_j \cdot (\boldsymbol{r}_i - \boldsymbol{r}_j) \tag{15}$$

To these values we add

$$\frac{(\boldsymbol{r}_i - \boldsymbol{r}_j)}{|\boldsymbol{r}_i - \boldsymbol{r}_j|} h \tag{16}$$

to i, and

$$-\frac{m_i}{m_j} \frac{(\boldsymbol{r}_i - \boldsymbol{r}_j)}{|\boldsymbol{r}_i - \boldsymbol{r}_j|} h \tag{17}$$

to j. Should the values (15) both be zero, we require

$$h(1 + m_i/m_j) > \tfrac{1}{2}(a_i + a_j) \tag{18}$$

so that contact is not sustained between the growing particles, and we make the choice whatever the value of Eq. (15)]

$$h = \frac{(a_i + a_j)}{(1 + m_i/m_j)} \tag{19}$$

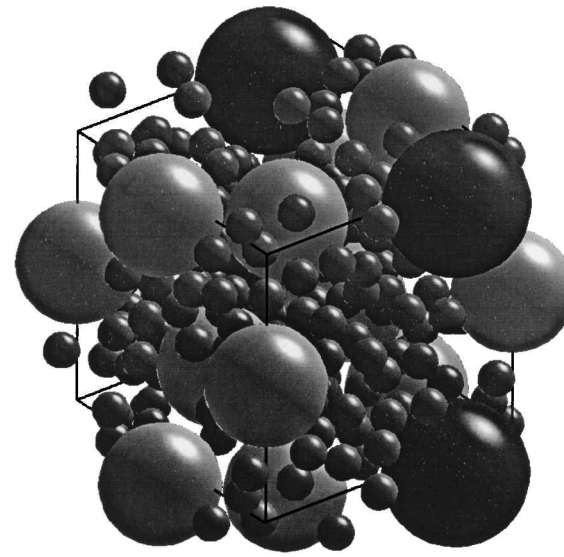

Fig. 2 Partial pack for a trimodal distribution.

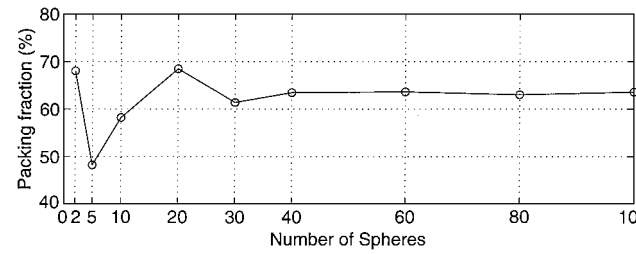

Fig. 3a. Monomodal packing fraction as a function of N.

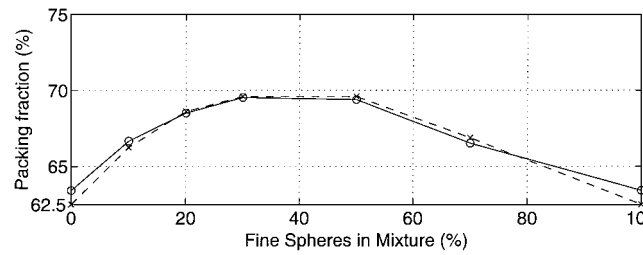

Fig. 3b. Packing fraction for the 7–20 bimodal mix, numerical (——) and experimental (- - -).[7]

As a consequence, the average speed of the particles increases with the number of collisions, and at various times it is useful to renormalize all of the velocities.

Before turning to detailed results, we show in Fig. 2 an intermediate pack for a trimodal distribution, a snapshot before the final packing is achieved. A packing movie can be seen at the website http://www.csar.uiuc.edu/~tlj/rocfire.html cited June 2000].

Results of the Packing Algorithm

Lubachevsky and Stillinger have reported results for single-sized particles.[8] They find that for $N = 1000$, the packing density $\rho = 0.63715960$, and that for $N = 8000$, $\rho = 0.63788205$. These results are close to the experimental values of McGeary.[7] Fortunately, accurate answers can be generated for much smaller values of N. We find that $\rho = 0.634266$ for $N = 40$ and that $\rho = 0.635362$ for $N = 100$, with little variation for $N > 40$ (Fig. 3a). Only for a modest number of spheres in the cube, with a corresponding modest number in any slice through the cube, can we realistically expect to calculate the associated combustion field.

Calculations using this algorithm have not previously been reported for bimodal packing. Figure 3b shows results that we have obtained for a mesh 7–mesh 20 mixture compared to McGeary's[7] data, and excellent agreement is achieved. The only other attempt to predict McGeary's data that we are aware of is reported in Ref. 10;

Table 2 Packing fractions for a mix of 20% mesh 7 and 80% mesh 30

No. of mesh 7	No. of mesh 30	ρ
20	542	0.7553
30	814	0.7278
40	1085	0.7428

reasonable agreement is achieved when high-order approximations in this theory are used, but only packing densities are reported, not morphologies.

Calculations for a mix consisting of 20% mesh 30 and 80% mesh 7 yield the results shown in Table 2. McGeary's result,[7] read from Fig. 1, is close to 74%, and so again, when we use 40 large spheres we get excellent agreement. Note that the total number of spheres (1125) is quite large, so that these computations are intensive. The number of small spheres required for a fixed fraction grows more rapidly than the inverse diameter cubed so that a mesh 70–mesh 6 mix, 20% fine, requires more than 10,000 particles.

Comments

Notwithstanding the agreement between the calculated results and McGeary's data,[7] a recent paper that only became available to us after the submission of this work makes clear that there are subtle issues in the study of random close packing (RCP).[11] To paraphrase Ref. 11, the idea that RCP is the highest possible density that a random sphere packing can attain is ill defined because one can achieve arbitrarily small increases in packing fraction at the expense of small increases in order. Thus, the packing fractions achieved by the Lubachevsky–Stillinger[8] protocol depend on the set of growth rates of the spheres: the smaller these rates the more ordered is the final pack, and the higher the packing density. Monomodal packing densities between 0.64 and 0.68 are reported in Ref. 11, the smaller figure being close to our results. This issue is unlikely to be relevant to the propellant application, where it is probably sufficient to avoid strongly ordered (lattice) states.

Propellant Data

A large body of propellant data has been reported by Miller.[12] Consider, for example, the propellant labeled SD-111-88-11. This consists of 45.26% by weight of 20-μm AP particles, 42.11% by weight of 6-μm AP particles. The size ratio is 3.333, not too different from the mesh 7–mesh 20 ratio of 3.4444. The percentage of fine particles is 48% and McGeary's data[7] (see Figure 3b) predict a packing fraction of approximately 0.70 in this case. If we take the specific gravity of AP to be 1.95 and that of the binder to be 1.01 (Ref. 13), the corresponding mass fraction is 0.818, compared to the actual value of 0.8737. Put another way, the actual volume fraction of AP is 0.782 compared to the predicted value (assuming perfect spheres of only two sizes) of 0.70, a significant difference. Various reasons for this discrepancy come to mind. The AP particles are not exactly 6 or 20 μm in diameter and cannot, in fact, be characterized by a single length because they are not spherical. Thus, variations in size about the mean value may account for the discrepancy, as may the deviations from sphericity. These questions can be explored by appropriate modification of the basic algorithm, and we plan to do this in the future. Despite this unresolved issue, we proceed with calculations relevant to this propellant.

We take 20 particles of diameter 20 μm and 688 particles of diameter 6 μm, so that the ratio of the volume of small to large is 0.9288 (cf. Miller's[12] ratio of 0.9304). We shall show the results of three packing calculations for different values of the seed that controls the random choices of the initial data. Figure 4 shows equally spaced slices through one of the packs generated in this way, with $\rho = 0.6807$. The separation between the slices is one-eighth of the cube's linear dimension. This dimension (scaled from the particle sizes) is 61.92 μm. (Thus, if the larger particles were 100 μm in diameter, the cube side would be 309.6 μm). The first and last slices in Fig. 4 correspond to the end faces and so are identical. In all of these calculations we have found it convenient to consider a cube of

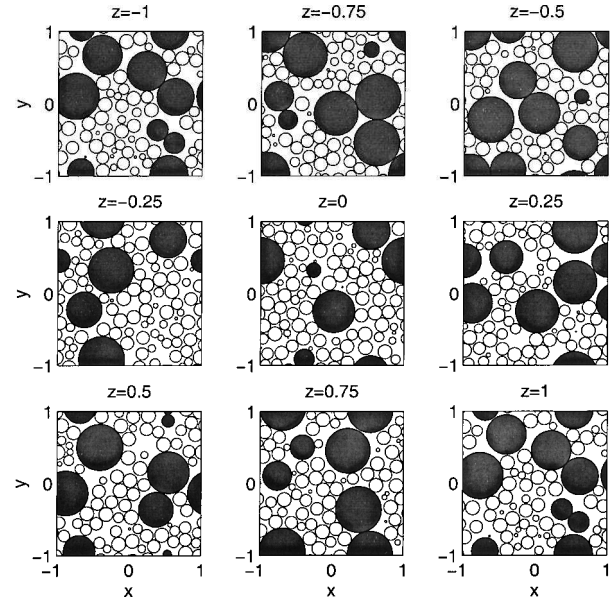

Fig. 4. Propellant slices for seed A; packing fraction = 0.6807.

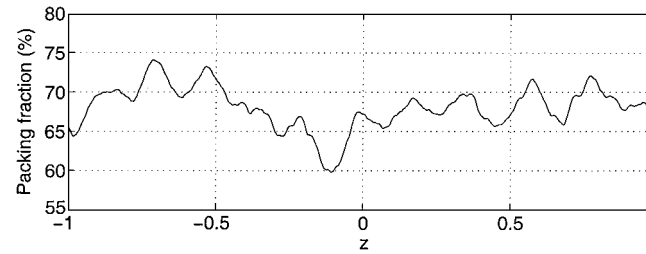

Fig. 5a. Variations in the area packing fraction with z for seed A.

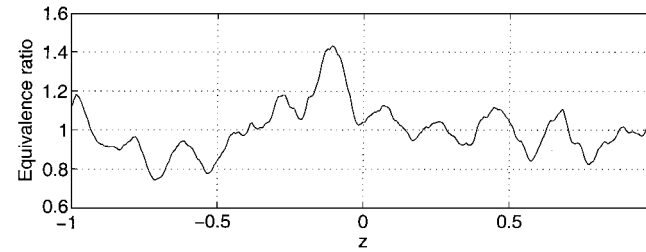

Fig. 5b. Corresponding variations in the equivalence ratio ϕ.

side 2, centered at the origin of axes, and this requires some minor rewording of our description of the algorithm.

Figure 5a shows variations in the area packing fraction as one proceeds through the cube. The integral average (area under the curve divided by 2) is 0.6807. An area equivalence ratio ϕ for each slice can be defined by the formula

$$\phi = \frac{\text{binder area}}{\text{AP area}} \cdot \frac{\text{AP volume}}{\text{binder volume}} \tag{20}$$

the volume ratio being 0.6807/0.3193. These variations are shown in Fig. 5b.

The integrated average of ϕ is 1.00515, close to 1 but not equal to 1, and we can understand this in the following fashion. The fractional AP area can be written as

$$A_{\mathrm{AP}} = 0.6807(1 + \epsilon) \tag{21}$$

Then, if we replace the fractional binder area by $1 - A_{\mathrm{AP}}$ and expand the formula (20) as a Taylor series in ϵ, we find

$$\phi = 1 + (1/0.3193)(-\epsilon + \epsilon^2 + \cdots) \tag{22}$$

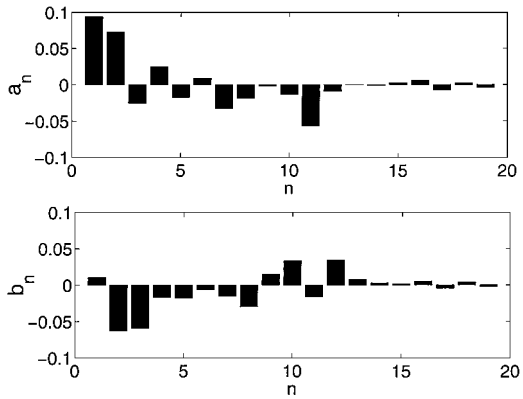

Fig. 6. Fourier series coefficients for the equivalence ratio of Fig. 5b.

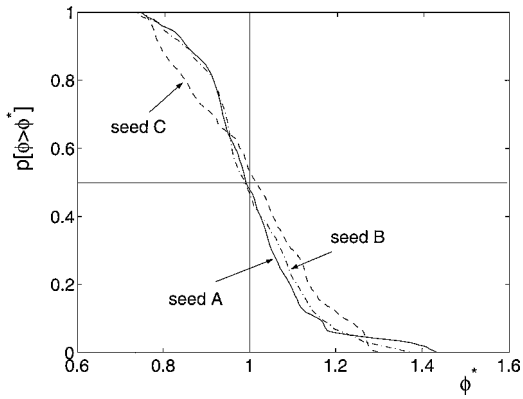

Fig. 7. Plot of $p\ \phi > \phi^*]$ vs ϕ^* for seed A (——), seed B (-·-), and seed C (- - -).

and because the integral of ϵ over the interval vanishes,

$$\frac{1}{2}\int_{-1}^{+1} \phi \, \mathrm{d}z = 1 + \frac{\frac{1}{2}}{0.3193}\int_{-1}^{+1} \epsilon^2 \, \mathrm{d}z + \mathcal{O}(\epsilon^3) \qquad (23)$$

where ϵ is roughly 0.05, and so it is clear why the integrated equivalence ratio is very close to 1 despite pointwise deviations that are as large as 40%.

The Fourier representation of ϕ is

$$\phi = \sum_{n=0}^{\infty} a_n \cos n\pi z + \sum_{n=1}^{\infty} b_n \sin n\pi z \qquad (24)$$

and the coefficients a_{1-19} and b_{1-19} are shown in Fig. 6 (a_0, essentially 1, is not shown). The small particles have a diameter $\simeq \frac{1}{10}$ of the cube side, corresponding to $n \simeq 10$, and there is some mode enhancement in that neighborhood. The larger particles have a diameter $\simeq \frac{1}{3}$ of the cube side, corresponding to $n = 3$, and the impact of these is also apparent. It might be thought that the strong $n = 1$ mode is a natural consequence of examining periodic cubes, but we shall see that this mode is not always significant.

The solid curve in Fig. 7 shows $p\ \phi > \phi^*]$, the probability that in any slice through the propellant the equivalence ratio is greater than ϕ^*; it is plotted against ϕ^*. The distance between the upper axis and the curve is $p\ \phi < \phi^*]$. Approximately one-half of the slices are fuel rich, one-half fuel lean, but the distribution is not symmetric. This is also apparent in the histogram of Fig. 8, which shows $p\ \phi^* - 0.025 < \phi < \phi^* + 0.025]$ for the discrete values of ϕ^* 0.7(0.05)1.5.

Figures 9–12 show the same information for a different choice of the random seed ($p\ \phi > \phi^*]$ is drawn in Fig. 7 as a dash–dot curve). The $n = 3$ and $n \simeq 10$ Fourier modes are again significant (Fig. 11). Remarkably, almost one-fourth of the slices have an equivalence ratio in the interval (0.925, 0.975) (Fig. 12).

Finally, Figs. 13–16 show the results for a third choice of the seed. The Fourier modes $n = 3$ and 10 are significant, but the mode $n = 1$ is not (Fig. 15). Note that for all three seeds (Figs. 6, 11, and 15) the $n = 2$ mode is always significant, for reasons that are not obvious to us. Note also that far fewer modes are significant for the third seed than for the other two. Perhaps not coincidentally, the histogram of Fig. 16 shows a much broader distribution than the other two, with all of the individual probabilities lying below 0.13, and 10 of 12 lying above 0.05. The curve in Fig. 7 for this case (dashed line) is the most symmetric of the three.

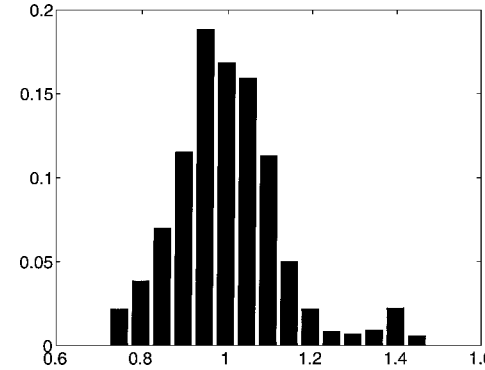

Fig. 8. Histogram of the equivalence ratio for seed A.

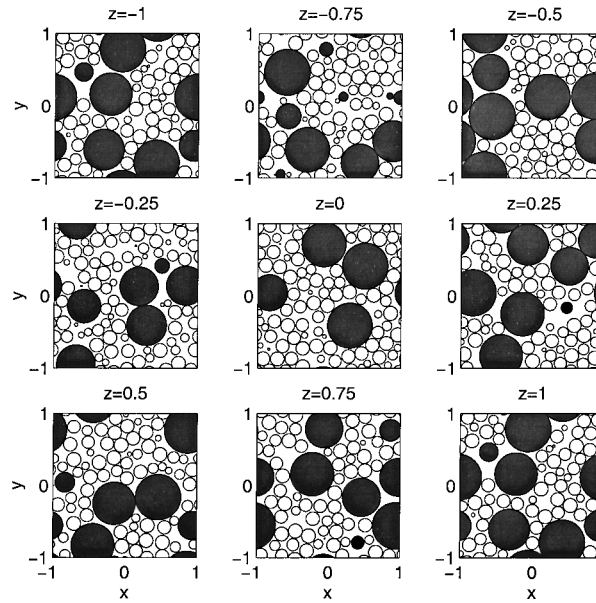

Fig. 9. Propellant slices for seed B; packing fraction = 0.6930.

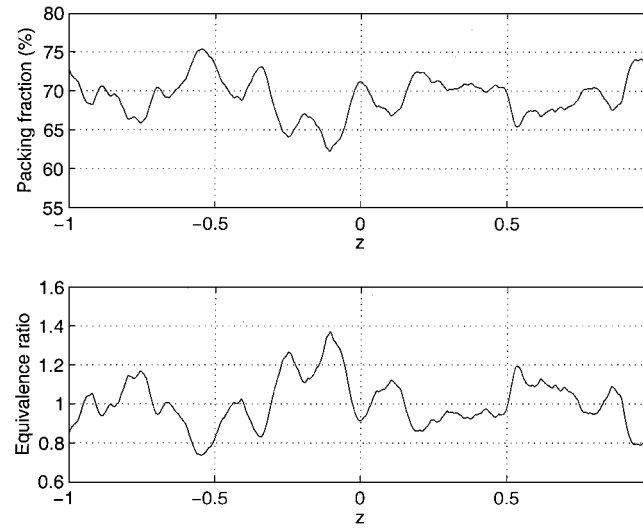

Fig. 10. Area packing fraction and equivalence ratio variations for seed B.

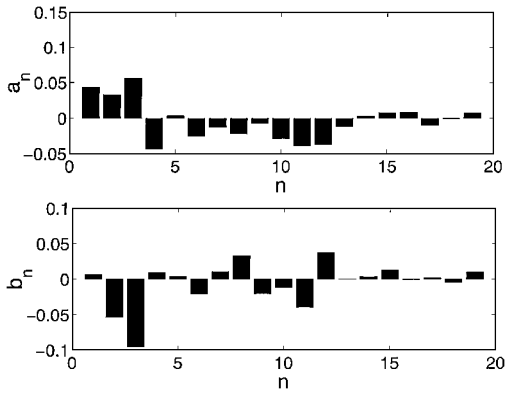

Fig. 11. Fourier coefficients of the equivalence ratio for seed B.

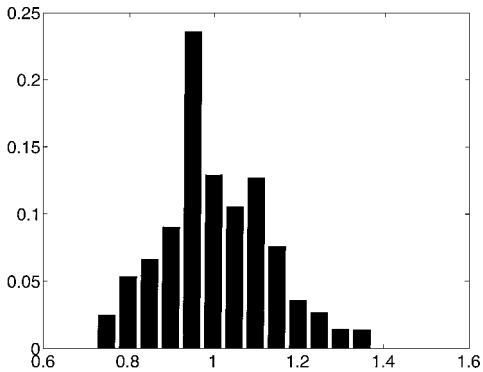

Fig. 12. Histogram of the equivalence ratio for seed B.

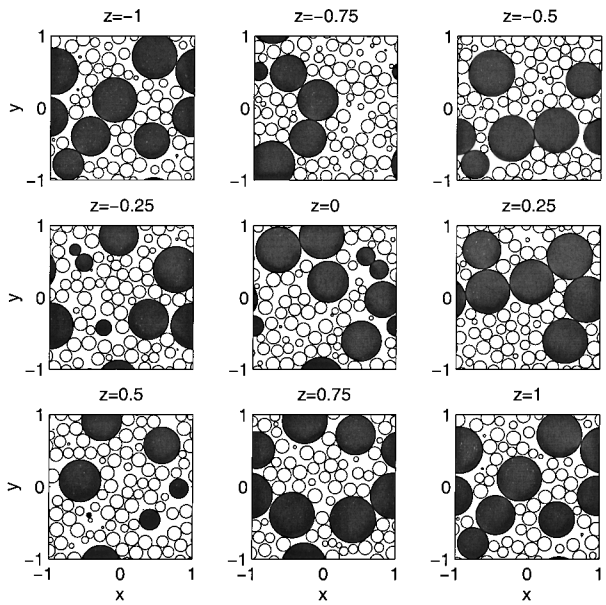

Fig. 13. Propellant slices for seed C; packing fraction = 0.6943.

Although the choice of three different seeds generates only three realizations of the propellant cube, it generates nine realizations of the set of propellant slices (burning faces) because each cube can be sliced in three different directions. We have shown results for which the slices are in the x–y plane; Fig. 17 shows a histogram for seed C for which the slices are in the y–z plane, a result quite different from Fig. 16 for the same seed.

What these results show collectively is that, apart from the persistence of the $n = 2$, 3, and $n \simeq 10$ modes in the Fourier analysis of the equivalence ratio, it is difficult to draw general conclusions. The product is random.

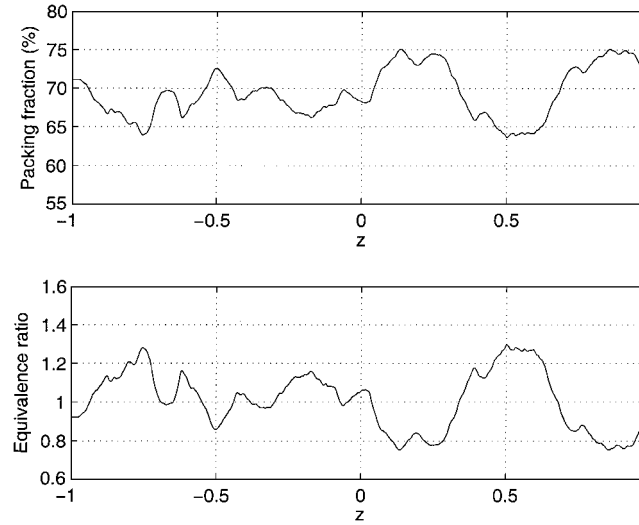

Fig. 14. Area packing fraction and equivalence ratio variations for seed C.

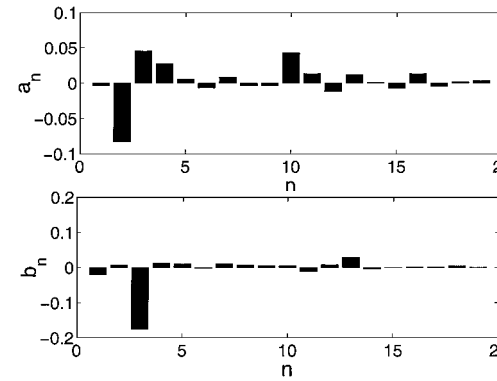

Fig. 15. Fourier coefficients of the equivalence ratio for seed C.

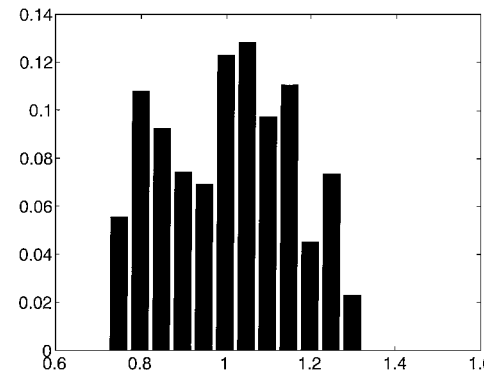

Fig. 16. Histogram of the equivalence ratio for seed C.

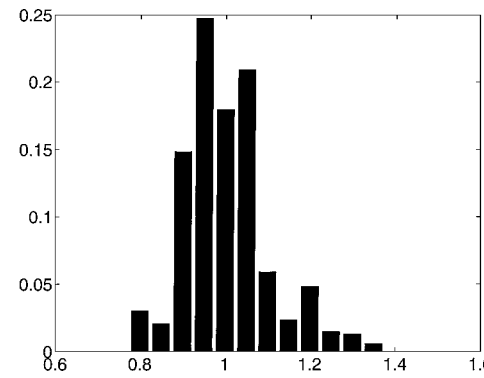

Fig. 17. Histogram of the equivalence ratio for seed C; slices in the y–z plane.

Table 3 Packing fractions for an Al/AP mix

Case	No. of large AP	No. of small AP	No. of Al	ρ_{AP}	ρ_{solids}	Cube size, (μm)
1	20	556	4	0.5848	0.7002	63.06
2	40	1111	7	0.6011	0.7049	78.72

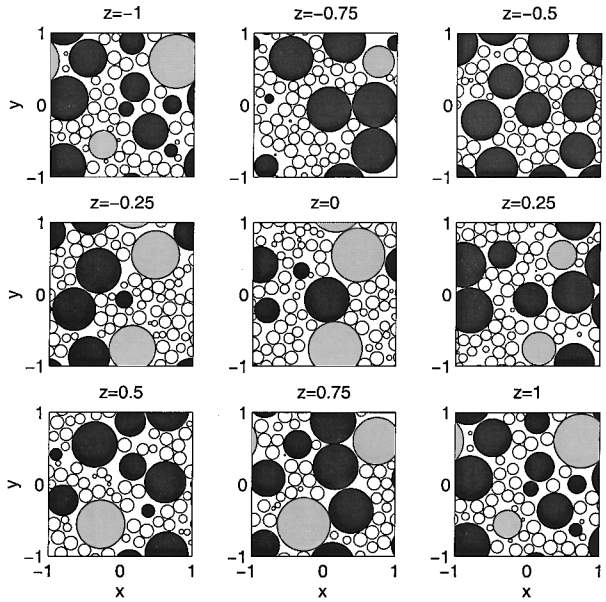

Fig. 18. Propellant slices with added aluminum, case 1.

Inclusion of Aluminum

When aluminum is included in the propellant mix, it will be necessary, in general, to account for three sets of particles: large AP, with some distribution about the mean, perhaps; small AP, also with some distribution; and aluminum. The propellant SD-1-88-13 described by Miller[12] contains 40% by weight of 20-μm AP particles, 30% by weight of 6-μm AP particles, and 18% by weight of 24-μm Al particles, so that the particles total 88% by weight. Assuming specific gravities of AP:1.95, Al:2.79, binder:1.01 (Ref. 13), the corresponding volume percentages are AP:66.2% and Al:11.9%, for a total of 78.1%.

We have carried out two calculations with the relative percentages of the various particles fixed at Miller's[12] values, to the extent possible for an integer number of particles. Results are shown in Table 3.

Again, the packing fractions achieved are short of the experimental values, probably for reasons that we have already described. If we lump the Al and large AP particles together, the percentage of fine particles compared to the total volume of particles is 57.6%, so that the packing fractions of approximately 70% that we get are again consistent with McGeary's[7] data. The discrepancy is not due to an inadequacy in the algorithm, it is a consequence of the choice of particle sizes and shape.

Figures 18–21 show propellant slices for the two cases, the corresponding variations of area fractions (AP and Al), and the equivalence ratio still defined by Eq. (20)]. Some of the slices contain no Al, and some slices contain as much as 20% Al.

Propellant Flames

Packing algorithms have a number of applications, but we have already made clear our interest in generating physically meaningful data that can be used in propellant flame calculations. Previous calculations have used a lattice pack,[5,6] but if one compares slices through such a propellant with the slices we show here (Figs. 4, 9, 13, 18, and 20), there are significant differences. It is well established by experiment that burning rates, pressure exponents, and other propellant burning characteristics are affected by the size and size distribution of the AP particles, and so the ability to construct realistic packs is important in any theoretical attempt to explain

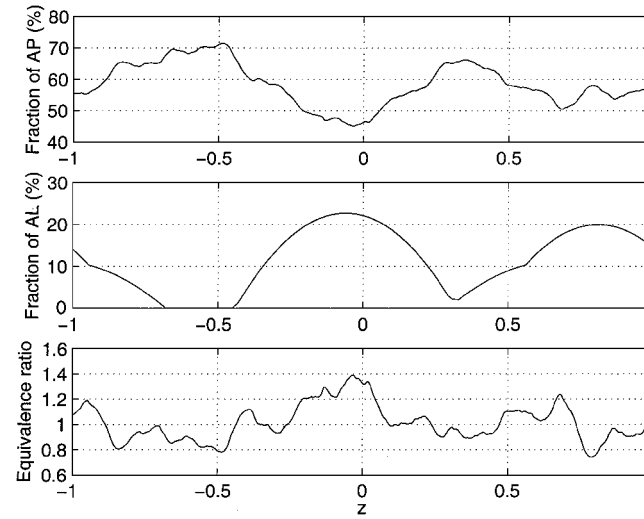

Fig. 19. Area packing fractions of AP and Al, equivalence ratio, case 1.

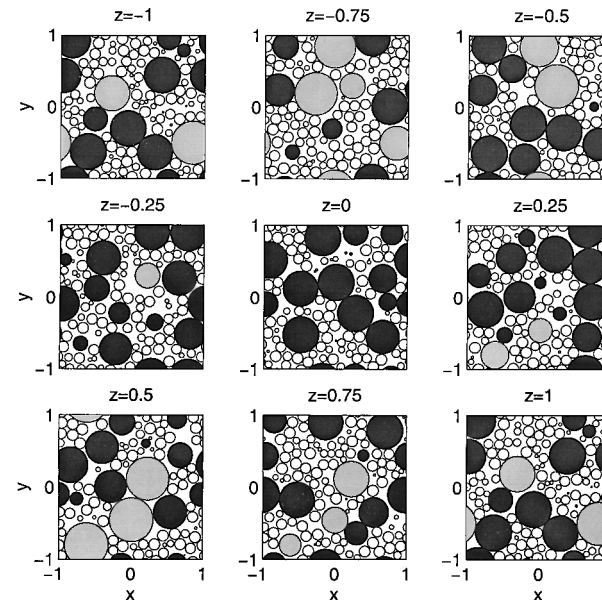

Fig. 20. Propellant slices with added aluminum, case 2.

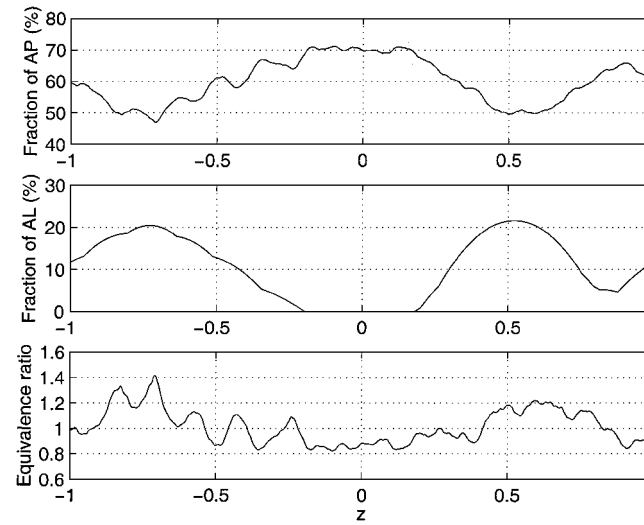

Fig. 21. Area packing fractions of AP and Al, equivalence ratio, case 2.

these effects. It is not our purpose to discuss flame calculations in detail, this must await another forum, but we shall give some hint of their nature, to put some purpose to the abstract structures discussed in the preceding sections.

Our first examination of the flames supported by slices like those of Figs. 4, 9, and 13 uses elementary ingredients: The propellant surface is flat; the surface temperature is uniform and assigned; the mass flux at the surface (associated with the regression) is uniform and assigned; an Oseen model is used in the gas phase with the convective operator replaced by $M(\partial/\partial z)$, where M is the mass flux (assumed uniform everywhere) and z is the distance measured normal to the surface; and simple one-step kinetics are adopted. These ingredients do not need to be defended, for they are only stepping stones to a better reality, but note that the Oseen model has been validated for one-dimensional periodic propellants supporting two-dimensional periodic flames: Calculations carried out using the Oseen model differ little from those carried out using the Navier–Stokes equations.[5,14,15]

There are two types of flame, the AP decomposition flame and the AP/binder flame. It is sometimes argued that the AP flame is so close to the surface that it can be accounted for as an exothermic sheet at the surface itself. In the context of the model, it then plays no direct role: The heat that it generates is indirectly accounted for by the specification of the surface temperature. Figure 22 is then typical of the reaction rate contours associated with the AP/binder reaction. This shows x–z slices through the field supported by the surface $z = -0.5$ of Fig. 4. These calculations are for a Peclet number of 20 (defined by the cube edge length and the mass flux) and reaction stoichiometry of 0.6807/0.3193, the volume stoichiometry of the cube. More details of the model applied in a simpler context may be found in Ref. 14.

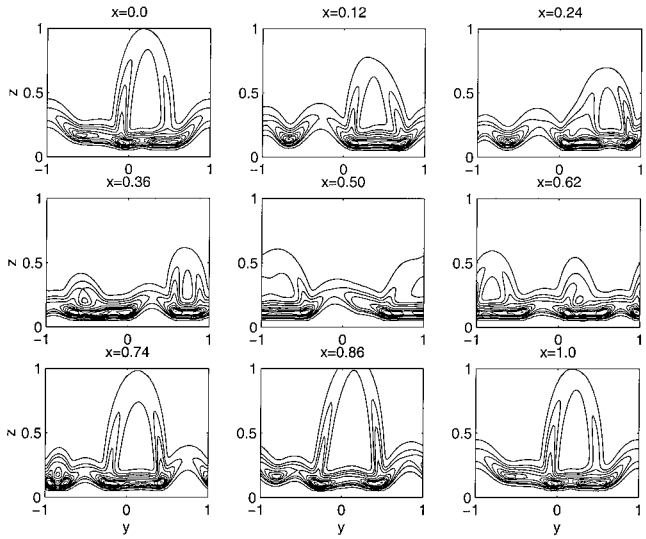

Fig. 22. Slices through the combustion field supported by the surface $z = -0.5$ of Fig. 4; reaction rate contours for the AP/binder reaction are shown, values 16, 12, 10, 8, 6, 4, 2, 1, 0.5, and 0.1.

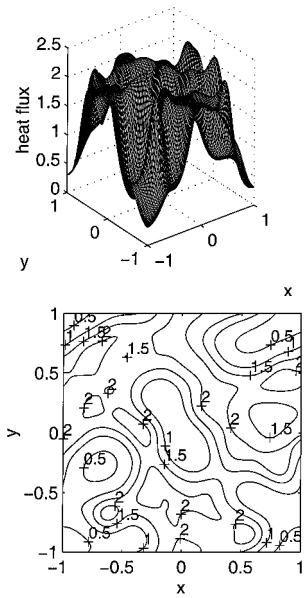

Fig. 23. Surface heat flux associated with the combustion field of Fig. 22.

Discrete diffusion flames are apparent (the Bunsen-flame shapes), but the important characteristics are the intense reaction zones at the base of these flames, edge structures and merged edge structures that are the source of the heat conducted to the surface. (Price has championed the importance of edge structures such as these, e.g., Lee et al.[4]) This heat flux is shown in Fig. 23 in both topographic form and in contour form. In due course we expect to calculate the nonuniform regression generated by this heat flux and link this regression in realistic fashion to chamber conditions.

Conclusions

In this paper it has been shown that the dynamic packing algorithm of Lubachevsky and Stillinger[8] can be used to generate propellant packs that promise to be of value in the numerical simulation of flames supported by heterogeneous propellants. In due course we expect to generate packs in which the AP size distribution mimics that of real propellants and to use these in the prediction of burning rates.

The number of particles that we have used for the sample calculations presented is quite modest (1000 or so), but when the use of a restricted set of possible collision partners is carefully implemented and collision times are stored, single-processor calculations for 10,000 particles can be accomplished in reasonable time. Because such a code is essentially linear in N, we expect to be able to carry out multiprocessor calculations for 100,000 particles or so. This will permit the explicit description of a pack with a wide range of sizes. It is possible that resolution issues for the flame calculations will require homogenization of the smaller particles with the binder to create an AP/binder mixture in which are imbedded pure AP particles.

Acknowledgments

This work was supported by the U.S. Department of Energy through the University of California under Subcontract B341494. In addition, J. Buckmaster is supported by the Air Force Office of Scientific Research. We are grateful to R. Bennett of Thiokol Corporation for helpful discussions about the nature of heterogeneous propellants and to R. Glick for his continuing encouragement.

References

[1] Kerstein, A. R., "Percolation Model of Polydisperse Composite Solid Propellant Combustion," *Combustion and Flame*, Vol. 69, No. 1, 1987, pp. 95–112.

[2] Murphy, J., and Krier, H., "Linear Pressure Coupled Frequency Response of Heterogeneous Solid Propellants," *Proceedings of the Combustion Institute*, Vol. 27, No. 2, 1998, pp. 2343–2350.

[3] Beckstead, M. W., Derr, R. L., and Price, C. F., "Model of Composite Solid-Propellant Combustion Based on Multiple Flames," *AIAA Journal*, Vol. 8, No. 12, 1970, pp. 2200–2207.

[4] Lee, S. T., Price, E., and Sigman, R. J., "Effect of Multidimensional Flamelets in Composite Propellant Combustion," *Journal of Propulsion and Power*, Vol. 10, No. 6, 1994, pp. 761–768.

[5] Buckmaster, J., and Jackson, T. L., "Flames Supported by Heterogeneous Propellants," AIAA Paper 2000-0306, Jan. 2000.

[6] Jackson, T. L., Buckmaster, J., and Hoeflinger, J., "3D Flames Supported by Heterogeneous Propellants," *Proceedings of the Combustion Institute*, Vol. 28 (to be published).

[7] McGeary, R. K., "Mechanical Packing of Spherical Particles," *Journal of the American Ceramic Society*, Vol. 44, No. 10, 1961, pp. 513–522.

[8] Lubachevsky, B. D., and Stillinger, F. H., "Geometric Properties of Random Disk Packings," *Journal of Statistical Physics*, Vol. 60, Nos. 5/6, 1990, pp. 561–583.

[9] Lubachevsky, B. D., Stillinger, F. H., and Pinson, E. N., "Disks vs Spheres: Contrasting Properties of Random Packings," *Journal of Statistical Physics*, Vol. 64, Nos. 3/4, 1991, pp. 501–524.

[10]Davis, I. L., and Carter, R. G., "Random Particle Packing by Reduced Dimension Algorithms," *Journal of Applied Physics*, Vol. 67, No. 2, 1990, pp. 1022–1029.

[11]Torquato, S., Truskett, T. M., and Debenedetti, P. G., "Is Random Close Packing of Spheres Well Defined?" *Physical Review Letters*, Vol. 84, No. 10, 2000, pp. 2064–2067.

[12]Miller, R. R., "Effects of Particle Size on Reduced Smoke Propellant Ballistics," AIAA Paper 82-1096, June 1982.

[13]Sutton, G. P., *Rocket Propulsion Elements*, 6th ed., Wiley, New York, 1992, p. 450.

[14]Jackson, T. L., and Buckmaster, J., "Nonpremixed Periodic Flames Supported by Heterogeneous Propellants," *Journal of Propulsion and Power*, Vol. 16, No. 3, 2000, pp. 498–504.

[15]Jackson, T. L., Buckmaster, J., and Hegab, A., "Periodic Propellant Flames and Fluid-Mechanical Effects," *Journal of Propulsion and Power*, Vol. 17, No. 2, 2001, pp. 371–379.

J. R. Bellan
Associate Editor